


Thermochemical nonequilibrium effects on high-enthalpy double-wedge flows

Cite as: Phys. Fluids **34**, 063607 (2022); <https://doi.org/10.1063/5.0094929>

Submitted: 07 April 2022 • Accepted: 24 May 2022 • Accepted Manuscript Online: 26 May 2022 • Published Online: 08 June 2022

 Qizhen Hong (洪启臻),  Jiaao Hao (郝佳傲), Ken Chun Kit Uy (黃駿傑), et al.



View Online



Export Citation



CrossMark

ARTICLES YOU MAY BE INTERESTED IN

[Characterization of reflected shock tunnel air conditions using a simple method](#)

Physics of Fluids **34**, 056103 (2022); <https://doi.org/10.1063/5.0089120>

[Effect of thermal nonequilibrium on the shock interaction mechanism for carbon dioxide mixtures on double-wedge geometries](#)

Physics of Fluids **34**, 026108 (2022); <https://doi.org/10.1063/5.0078233>

[Development of a stagnation streamline model for thermochemical nonequilibrium flow](#)

Physics of Fluids **32**, 046102 (2020); <https://doi.org/10.1063/5.0003247>

Physics of Fluids
Special Topic: Cavitation

Submit Today!

Thermochemical nonequilibrium effects on high-enthalpy double-wedge flows

Cite as: Phys. Fluids **34**, 063607 (2022); doi: 10.1063/5.0094929

Submitted: 7 April 2022 · Accepted: 24 May 2022 ·

Published Online: 8 June 2022



View Online



Export Citation



CrossMark

Qizhen Hong (洪启臻),^{1,2,3} Jiaao Hao (郝佳傲),^{1,a)} Ken Chun Kit Uy (黃駿傑),¹ Chih-Yung Wen (溫志湧),¹
and Quanhua Sun (孙泉华)^{2,3}

AFFILIATIONS

¹Department of Aeronautical and Aviation Engineering, The Hong Kong Polytechnic University, Kowloon, Hong Kong

²State Key Laboratory of High Temperature Gas Dynamics, Institute of Mechanics, Chinese Academy of Sciences, 100190 Beijing, China

³School of Engineering Science, University of Chinese Academy of Sciences, Beijing 100049, China

^{a)}Author to whom correspondence should be addressed: jiaao.hao@polyu.edu.hk

ABSTRACT

A hypersonic laminar flow over double wedges with a fixed forward angle of 15° and varied aft angles is studied using computational fluid dynamics and global stability analysis (GSA) at a free-stream Mach number of 12.82 and a total enthalpy of 21.77 MJ/kg. The specific total enthalpy is high enough to trigger evident vibrational excitation and air chemistry. To assess the effects of thermal and chemical nonequilibrium, three different thermochemistry models of air are considered, including frozen, thermal nonequilibrium, and thermochemical nonequilibrium gases. Two-dimensional base-flow simulations indicate that the onset of incipient and secondary separation is insensitive to the inclusion of thermochemistry, although the size of the separation region is substantially reduced. GSA is then performed on the base flows and identifies a three-dimensional stationary global instability beyond a critical aft angle, which is also insensitive to thermochemical nonequilibrium. The criterion of the global stability boundary established for the supersonic flow over compression corners in a calorically perfect gas in terms of a scaled deflection angle [Hao *et al.*, “Occurrence of global instability in hypersonic compression corner flow,” *J. Fluid Mech.* **919**, A4 (2021)] is, thus, extended to high-enthalpy conditions.

Published under an exclusive license by AIP Publishing. <https://doi.org/10.1063/5.0094929>

I. INTRODUCTION

During the flight of a hypersonic vehicle, the shock-wave/boundary-layer interaction (SWBLI) is an important flow phenomenon.¹ At a high total enthalpy, the translational temperature across a strong shock wave is large enough to cause vibrational excitation, dissociation, electronic excitation, and ionization, which occur at time-scales comparable to the flow characteristic time. How these thermochemical nonequilibrium (TCN) processes modify the characteristics of SWBLI has attracted much attention.

The flow physics of high-enthalpy SWBLI have been studied by numerical and experimental means using many canonical configurations, such as shock impingement on a flat plate, compression corners, double wedges, double cones, etc. Furumoto *et al.*² numerically studied a two-dimensional SWBLI on a flat plate with three thermochemistry models: a perfect gas with frozen vibrational and chemical modes, a vibrationally excited but chemically frozen gas, and a vibrationally and chemically excited gas. The thermochemical nonequilibrium effects were found to reduce the size of the separation bubble and the surface

peak heating. For the vibrationally and chemically excited gas, further increasing the total enthalpy resulted in a smaller separation bubble. The hypersonic flow over a compression corner was experimentally studied by Mallinson *et al.*³ in the T3 shock tunnel at three total enthalpies ranging from 2.8 to 19.0 MJ/kg. The separation pressure coefficient, incipient separation angle, and peak heating agreed well with the experimental and theoretical results at low enthalpies. High-enthalpy experiments of nitrogen flow over double wedges were conducted by Olejniczak *et al.* in the T5 shock tunnel.⁴ Their companion numerical simulation using standard thermochemical models significantly underpredicted the size of the separation region. In addition, the numerical results were found to be sensitive to the equilibrium and nonequilibrium dissociation rates of nitrogen.

A series of double-cone experiments was conducted in the LENS I reflected shock tunnel at Calspan—University of Buffalo Research Center (CUBRC) at various flow conditions.⁵ In particular, several cases were designed at the same Mach number and Reynolds number but at different total enthalpies to address the thermochemical

nonequilibrium effects. The experiments showed that the size of the separation region first decreased and then increased as the total enthalpy was increased, whereas the computational fluid dynamics (CFD) predictions⁶ monotonically decreased. Meanwhile, the size of the separation bubble was significantly underestimated, particularly at high total enthalpies. The unusual behavior of the experiments may be due to the existence of vibrational and chemical nonequilibrium in the free-stream of the reflected shock tunnel.⁷

To provide a relatively clean free-stream environment without stagnating the test gas, a new set of double-cone experiments was conducted in the LENS XX expansion tunnel at CUBRC.⁸ Kianvashrad and Knight⁹ simulated the double-cone flows assuming thermally perfect, vibrationally excited but chemically frozen, and vibrationally and chemically excited gases. In accordance with Furumoto *et al.*,² the inclusion of air chemistry yielded a smaller separation region. Surprisingly, the separation bubble predicted by the vibrational equilibrium model was larger than the vibrational nonequilibrium counterpart. Holloway *et al.*¹⁰ examined the double-cone flows using the popular Park model¹¹ and a modified Marrone–Treanor model¹² based on high-fidelity quantum chemistry data. The two vibration–dissociation coupling models generated similar flowfields and surface quantities. Gao *et al.*¹³ further considered the most up-to-date vibrational relaxation times of air species along with the modified Marrone–Treanor model. For the highest enthalpy case, the separation region was enlarged by 17.9% compared to that predicted by the Park model. Despite these efforts, large discrepancies still exist between CFD and the experiments.

The aforementioned numerical studies only considered two-dimensional/axisymmetric laminar flows. In fact, different types of flow instability may occur in SWBLI, e.g., the first and second modes in the incoming boundary layer, global instability of the separation bubble, pulsation mode of the shock interaction system, etc. Understanding thermochemical nonequilibrium effects on these instabilities is critical to understand the breakdown of laminar interactions at high enthalpies.

Regarding the convective first and second modes, Malik and Anderson¹⁴ investigated Mach 10 and 15 flows over a flat plate using linear stability theory (LST). Thermochemical equilibrium stabilized the first mode but destabilized the second mode compared to the assumption of a calorically perfect gas. Hudson *et al.*¹⁵ further considered thermal and chemical nonequilibrium in both mean flow and LST and found that the second-mode instability in the nonequilibrium flow did not differ greatly from that in the equilibrium flow. More recently, Chen *et al.*¹⁶ investigated a Mach 20 wedge flow using parabolized stability equations with thermochemical nonequilibrium effects, which affected the boundary-layer instabilities mainly through the mean flow rather than the disturbances.

Recent studies have shown that the intrinsic instability of SWBLI can induce flow three-dimensionality both inside the separation region and downstream of reattachment, which is frequently accompanied by low-frequency unsteadiness.^{17–23} To date, only the calorically perfect gas model has been considered. The global stability of high-enthalpy SWBLI remains to be understood. To this end, the hypersonic flow over double wedges with varied aft angles is investigated using CFD and global stability analysis (GSA) with different thermochemistry models of air to reveal the thermochemical nonequilibrium effects on the base-flow properties and the global stability. The results are then interpreted according to the classical triple-deck theory.

II. GOVERNING EQUATIONS

In this study, Park's two-temperature model¹¹ is used to describe the thermochemical nonequilibrium processes, which assumes that the translational and rotational energy modes are in equilibrium corresponding to a translational-rotational temperature T_{tr} and that the vibrational energy of molecules and the electronic excitation energy are described by a Boltzmann distribution in terms of a vibrational-electronic temperature T_{ve} . The flow governing equations are the conservation equations of species mass, mixture momentum, total energy, and vibrational-electronic energy in the following form:

$$\frac{\partial \mathbf{U}}{\partial t} + \frac{\partial (\mathbf{F} - \mathbf{F}_v)}{\partial x} + \frac{\partial (\mathbf{G} - \mathbf{G}_v)}{\partial y} + \frac{\partial (\mathbf{H} - \mathbf{H}_v)}{\partial z} = \mathbf{\Omega}, \quad (1)$$

where $\mathbf{U} = [\rho_i, \rho u, \rho v, \rho w, \rho e, \rho e_{ve}]^T$ is the vector of conserved variables, and the vectors of convective and diffusive fluxes and the source terms are given by

$$\mathbf{F} = \begin{bmatrix} \rho_i u \\ \rho u^2 + p \\ \rho uv \\ \rho uw \\ (\rho e + p)u \\ \rho e_{ve} u \end{bmatrix}, \quad \mathbf{F}_v = \begin{bmatrix} -J_{i,x} \\ \tau_{xx} \\ \tau_{xy} \\ \tau_{xz} \\ u\tau_{xx} + v\tau_{xy} + w\tau_{xz} - q_{tr,x} - q_{ve,x} - \sum_{i=1}^{ns} J_{i,x} h_i \\ -q_{ve,x} - \sum_{i=mol.} J_{i,x} e_{ve,i} \end{bmatrix}, \quad (2)$$

$$\mathbf{\Omega} = \begin{bmatrix} \omega_i \\ 0 \\ 0 \\ 0 \\ 0 \\ \omega_{ve} \end{bmatrix}.$$

Vectors \mathbf{G} , \mathbf{H} , \mathbf{G}_v , and \mathbf{H}_v can be expressed analogously. In these expressions, ρ_i is the density of species i ; p is the pressure; u , v , and w are the flow velocities in the x , y , and z directions, respectively; τ is the viscous stress tensor modeled based on a Newtonian fluid and the Stokes hypothesis; q_{tr} and q_{ve} are the translational-rotational and vibrational-electronic heat fluxes modeled according to Fourier's law; J_i is the diffusion flux of species i modeled according to the modified Fick's law;²⁴ e is the specific total energy of the mixture; e_{ve} is the specific vibrational-electronic energy of the mixture; ω_i is the mass production rate of species i ; and ω_{ve} is the source term of the vibrational-electronic energy equation.

The species viscosities and thermal conductivities are evaluated using Blottner's curve fits²⁵ and the Eucken formula,²⁶ respectively. The viscosity and thermal conductivity of the mixture are then calculated using Wilke's mixing rule.²⁷ The species diffusion coefficients are obtained by assuming a constant Lewis number of 1.4.

Given the low degree of ionization at the considered flow conditions, only the five neutral air species (N, O, N₂, O₂, and NO) are considered. Park's 1990 chemical reaction model¹¹ is used to calculate the equilibrium forward rate coefficients, while the backward rate coefficients are obtained using the equilibrium constants. To consider the effects of vibrational nonequilibrium on dissociation rates, the geometric average of T_{tr} and T_{ve} with the power of 0.5 is taken as the controlling temperature of dissociation reactions.

The harmonic oscillator model is used to evaluate the vibrational energy, and only the first two electronic levels of each species are considered for the electronic energy. The source term ω_{ve} can be further decomposed into ω_{t-v} and $\omega_{chem,v}$. The term ω_{t-v} represents the energy transfer between the translational mode of particles and the vibrational mode of molecules, which is evaluated using the Landau–Teller model²⁶ as

$$\omega_{t-v} = \sum_{i=mol.} \rho_i \frac{e_{ve,i}(T_{tr}) - e_{ve,i}(T_{ve})}{\tau_{v,i}}. \quad (3)$$

The vibrational relaxation times $\tau_{v,i}$ are obtained by combining the Millikan–White expression²⁸ and Park's high-temperature correction¹¹ as

$$\tau_{v,i} = \tau_{v,i}^{MW} + (\sigma_i c_i n_i)^{-1}, \quad (4)$$

where σ_i and c_i denote the effective cross section and the average molecular velocity of species i and n_i is the number density of species i . $\tau_{v,i}^{MW}$ is modeled by the Millikan–White expression²⁸ as

$$\tau_{v,i}^{MW} = \frac{101325}{p} \frac{\sum_{s=1}^{ns} n_s \exp \left[A_{i-s} \left(T_{tr}^{-1/3} - B_{i-s} \right) - 18.42 \right]}{\sum_{s=1}^{ns} n_s}, \quad (5)$$

where A_{i-s} and B_{i-s} are the Millikan–White parameters computed by standard definitions.²⁸ The term $\omega_{chem,v}$ is the production rate of

vibrational energy due to molecular recombination and dissociation, which is modeled by assuming that molecules are created or destroyed with the average vibrational energy²⁹ as

$$\omega_{chem,v} = \sum_{i=mol.} \omega_i e_{ve,i}. \quad (6)$$

As demonstrated by Holloway *et al.*¹⁰ and Gao *et al.*,¹³ the effects of different vibration–dissociation coupling models on double-cone flows were weak at flow conditions similar to this study. Therefore, only the popular Park model¹¹ is used here. As the total enthalpy is further increased, more physically consistent vibration–dissociation coupling models,^{30–32} the vibrational state-to-state approach,³³ or the direct molecular simulation method³⁴ should be adopted to increase the predictive accuracy.

Three different thermochemistry models are considered in this study, including the frozen (labeled Fr), thermal nonequilibrium (labeled TN), and thermochemical nonequilibrium (labeled TCN) flow models. The Fr model is equivalent to a calorically perfect gas. The TN model considers vibrational excitation with no chemical reactions, whereas the TCN model includes all finite-rate processes.

III. COMPUTATIONAL DETAILS

A. Geometric configuration and flow conditions

The double-wedge configuration (see Fig. 1) considered in this study has a first wedge with a half angle of $\theta_1 = 15^\circ$ and a second wedge with various angles ($\theta_2 = 25^\circ$ – 55°). The angle between the first and second wedges is denoted by $\alpha = \theta_2 - \theta_1$. Hereafter, different cases will be labeled Fr- α , TN- α , and TCN- α . The surface lengths of the first and second wedges are equal to $L = 100$ mm, which is taken as the characteristic length of the flow. The coordinate system is constructed with the origin at the leading edge, the x -axis along the horizontal direction, and the y -axis along the vertical direction.

The free-stream conditions are given as follows: $M_\infty = 12.82$, $\rho_\infty = 9.64 \times 10^{-4}$ kg/m³, $T_\infty = 652$ K, $u_\infty = 6497$ m/s, $Re_\infty = 2.0 \times 10^5$ m⁻¹, and $h_0 = 21.77$ MJ/kg, which are taken from the recent double-cone experiments of Holden *et al.*⁸ conducted in the LENS XX expansion tunnel. The test gas was equilibrium air composed of 76.5% N₂ and 23.5% O₂ by mass fraction.

Two typical flow structures are shown in Fig. 1. For the TCN-26° case [see Fig. 1(a)], an oblique shock (OS) is generated at the leading

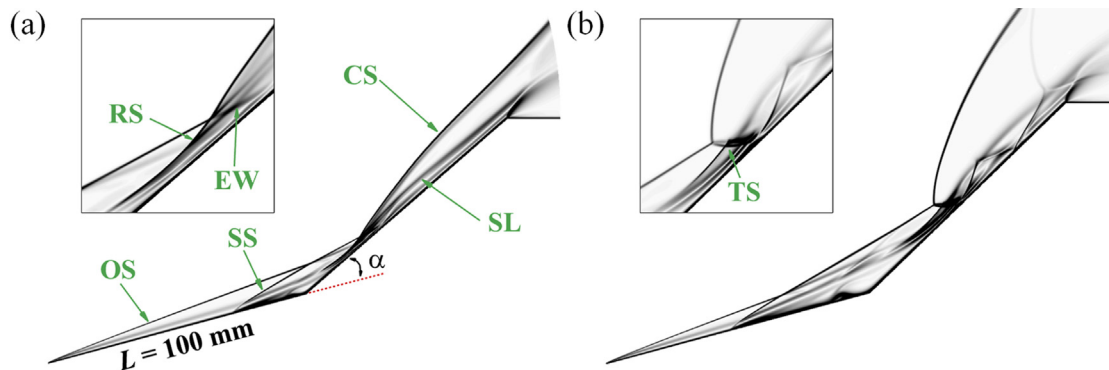


FIG. 1. Typical flow structures for (a) TCN-26° and (b) Fr-29°. CS: curved shock; EW: expansion wave; OS: oblique shock; RS: reattachment shock; SS: separation shock; SL: slip line; TS: transmitted shock.

edge of the first wedge, and a curved shock (CS) is induced by the second wedge. The adverse pressure gradient caused by the flow deflection is large enough to induce a separation region near the corner. A separation shock (SS) is generated and intersects the OS and CS successively. The flow structure of the TCN-26° case belongs to Edney's type VI shock interaction,³⁵ featuring a slip line (SL) and an expansion wave (EW). In contrast, the flow structure of the Fr-29° case [see Fig. 1(b)] resembles Edney's type V shock interaction.³⁶ The interaction between the SS and CS generates a transmitted shock (TS), which impinges the solid surface and undergoes a regular reflection. The TS also intersects the reattachment shock (RS) induced by the separation bubble.

B. Base-flow simulations

The two-dimensional base-flow simulations are performed using an in-house multiblock parallel finite-volume solver called PHAROS.^{37,38} The modified Steger–Warming scheme³⁹ is used to calculate the inviscid fluxes, which is extended to a higher order by the monotone upstream-centered schemes for conservation law reconstruction.⁴⁰ The viscous fluxes are computed using the second-order central difference. An implicit line relaxation method⁴¹ is employed for time marching.

The boundary conditions for the base-flow simulations are specified as follows: the free-stream conditions given in Sec. III A are specified at the inflow boundary; a first-order extrapolation is applied at the outflow boundary; a no-slip velocity condition is implemented at the wall, which is assumed to be isothermal for both T_{tr} and T_{ve} . The wall temperature is set to 300 K, corresponding to a wall-to-total temperature ratio T_w/T_0 of 0.0136. In addition, the solid surface is assumed to be noncatalytic.

Numerical simulations are run with a constant Courant–Friedrichs–Lewy number of 10^3 until iterative convergence. For all cases, numerical convergence is achieved under the criteria that the L_2 norm of the density residual is reduced by at least eight orders of magnitude and the distributions of surface quantities no longer change in successive iterations.

Computational grids over the first and second wedges are constructed with three levels of refinement, including 300×150 (coarse), 500×250 (medium), and 900×450 (fine), in the streamwise and wall-normal directions. Additional 80 streamwise points are placed on the plateau section downstream of the expansion corner. The normal spacing at the wall is set to 5×10^{-7} m to ensure that the grid Reynolds number is less than one. Figure 2 compares the distributions of the skin friction coefficient C_f , surface Stanton number St , and surface pressure coefficient C_p obtained on the different grids for the TCN-26° case. Here, C_f , St , and C_p are defined by

$$C_f = \frac{\tau_w}{0.5\rho_\infty u_\infty^2}, \quad St = \frac{q_w}{0.5\rho_\infty u_\infty^3}, \quad C_p = \frac{p_w}{0.5\rho_\infty u_\infty^2}, \quad (7)$$

where τ_w , q_w , and p_w are the surface shear stress, heat flux, and pressure, respectively. Given that the distributions obtained on the medium and fine grids almost overlap, the fine grid is used for the base-flow simulations.

C. Global stability analysis

It is assumed that \mathbf{U} can be decomposed into a two-dimensional steady solution and a three-dimensional small-amplitude perturbation as

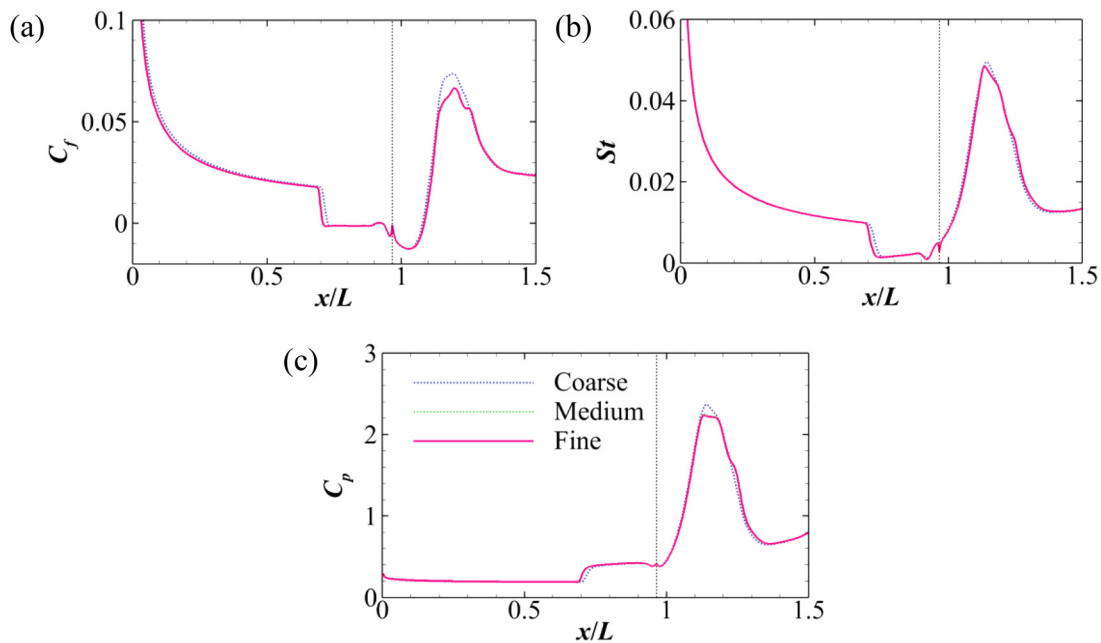


FIG. 2. Distributions of the (a) skin friction coefficient, (b) surface Stanton number, and (c) surface pressure coefficient obtained on three different grids for TCN-26°. The vertical line indicates the location of the corner.

$$\mathbf{U}(x, y, z, t) = \bar{\mathbf{U}}(x, y) + \mathbf{U}'(x, y, z, t). \quad (8)$$

The governing equations of \mathbf{U}' are obtained by linearizing Eq. (1) and discretized using a second-order finite-volume method. The linearized inviscid fluxes are computed using the modified Steger–Warming scheme near discontinuities and a central scheme in smooth regions to reduce numerical dissipation. The linearized viscous fluxes are calculated using the second-order central difference.

Vector \mathbf{U}' is further assumed to be in the following modal form:

$$\mathbf{U}'(x, y, z, t) = \hat{\mathbf{U}}(x, y) \exp \left[-i(\omega_r + i\omega_i)t + i\frac{2\pi}{\lambda_z}z \right], \quad (9)$$

where $\hat{\mathbf{U}}$ is the two-dimensional eigenfunction, ω_r is the angular frequency, ω_i is the growth rate, and λ_z is the spanwise wavelength. Substituting Eq. (9) into the linearized governing equations leads to an eigenvalue problem as

$$\bar{\mathbf{A}}\hat{\mathbf{U}} = (\omega_r + i\omega_i)\hat{\mathbf{U}}, \quad (10)$$

where $\bar{\mathbf{A}}$ is the global matrix (a large sparse matrix) composed of Jacobians of the inviscid and viscous fluxes and source terms. The eigenvalue problem is solved for a given λ_z using the shift-and-invert implicitly restarted Arnoldi method implemented in ARPACK.⁴² Specifically, the inversion step is achieved via lower–upper decomposition of the shifted global matrix implemented in Super-LU.⁴³

The boundary conditions for the GSA are specified as follows: all the perturbations are set to zero at the inflow boundary; a simple extrapolation is used at the outflow boundary; and the boundary conditions at the wall are given by

$$\hat{u} = \hat{v} = \hat{w} = \hat{T}_{tr} = \hat{T}_{ve} = \frac{\partial \hat{p}}{\partial n} = 0. \quad (11)$$

Furthermore, sponge layers are placed near the inflow and outflow boundaries of the computational domain to ensure no reflection of perturbations.⁴⁴

Lower–upper decomposition of the global matrix is computationally expensive in terms of memory usage, particularly for thermochemical nonequilibrium flows with five more variables than calorically perfect gas flows. To reduce the computational burden, the GSA is performed on the base flows obtained on the medium grid (500 × 250). Grid independence was verified by comparing the eigenvalue spectra at the most unstable spanwise wavelength $\lambda_z/L = 0.1337$ (discussed in Sec. IV B) obtained on the medium and fine grids for the TCN-26° case, as shown in Fig. 3.

IV. RESULTS

A. Base flows

As α is increased from a small value (the minimum increment of α is 1°), the double-wedge flow undergoes several stages: no flow separation, a primary separation bubble beyond incipient separation, a secondary separation bubble beneath the primary bubble and multiple vortices. In this process, the shock interaction transitions from Edney's type VI to type V.³⁵

For the Fr model, the critical angle is 13°–14° for incipient separation, 25°–26° for secondary separation, and 28°–29° for shock interaction type transition. Figure 4 shows the contours of the density gradient magnitude for four typical values of α obtained using the Fr

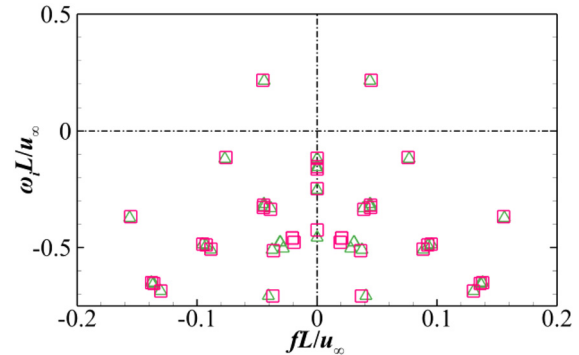


FIG. 3. Eigenvalue spectra obtained on different grids for TCN-26° at the most unstable spanwise wavelength $\lambda_z/L = 0.1337$. Triangles: medium grid; squares: fine grid.

model. The streamlines in the separation region and the sonic lines are also plotted. At $\alpha = 14^\circ$, a small separation bubble (almost invisible from the figure) forms near the corner, which marks the onset of incipient separation. The separation bubble grows as α is increased to 20°. At $\alpha = 26^\circ$, secondary separation first occurs on the first wedge and distorts the primary bubble. For these three angles, the shock structures belong to Edney's type VI interaction. At $\alpha = 29^\circ$, the secondary bubble grows, and the primary bubble splits into two vortices. Meanwhile, the shock structure transitions into Edney's type V interaction with a locally subsonic flow region behind the strong portion of the curved shock.

For the TN model, the critical angles for incipient separation, secondary separation, and shock interaction type transition are 13°–14°, 24°–25°, and 32°–33°, respectively. For the TCN model, the three critical angles are 13°–14°, 25°–26°, and 39°–40°. Compared with the Fr model, the onset of incipient and secondary separation remains almost unchanged with the inclusion of vibrational excitation and air chemistry. Similar observations regarding incipient separation were made by Mallinson *et al.*³ Therefore, the flow structures resemble those shown in Fig. 4 at relatively small angles except that the curved shock lies closer to the second wedge and the size of the separation bubble is reduced. This is because endothermic vibrational excitation and dissociation behind the curved shock decrease the translational temperature and, thus, increase the mixture density. Similar effects occur in the separation region.¹ The smaller shock standoff distance postpones the transition of the shock interaction type. The contours of the density gradient magnitude for the TN-33° and TCN-40° cases beyond the shock interaction type transition are shown in Fig. 5. For the TCN model, the separation region fragments into multiple vortices at $\alpha = 40^\circ$ while remaining steady, which cannot be observed for the Fr model. In fact, the Fr flow becomes unsteady due to an inviscid pulsation mechanism⁴⁵ when the aft angle exceeds the shock detachment angle of the second wedge with respect to M_∞ ($\alpha \approx 30^\circ$). In other words, thermochemical nonequilibrium delays the onset of pulsation mode.

Figure 6 compares the contours of nondimensional translational-rotational temperature for the Fr, TN, and TCN models at $\alpha = 26^\circ$. The thermochemical nonequilibrium processes distribute energy from the translational-rotational mode to the vibrational-electronic mode

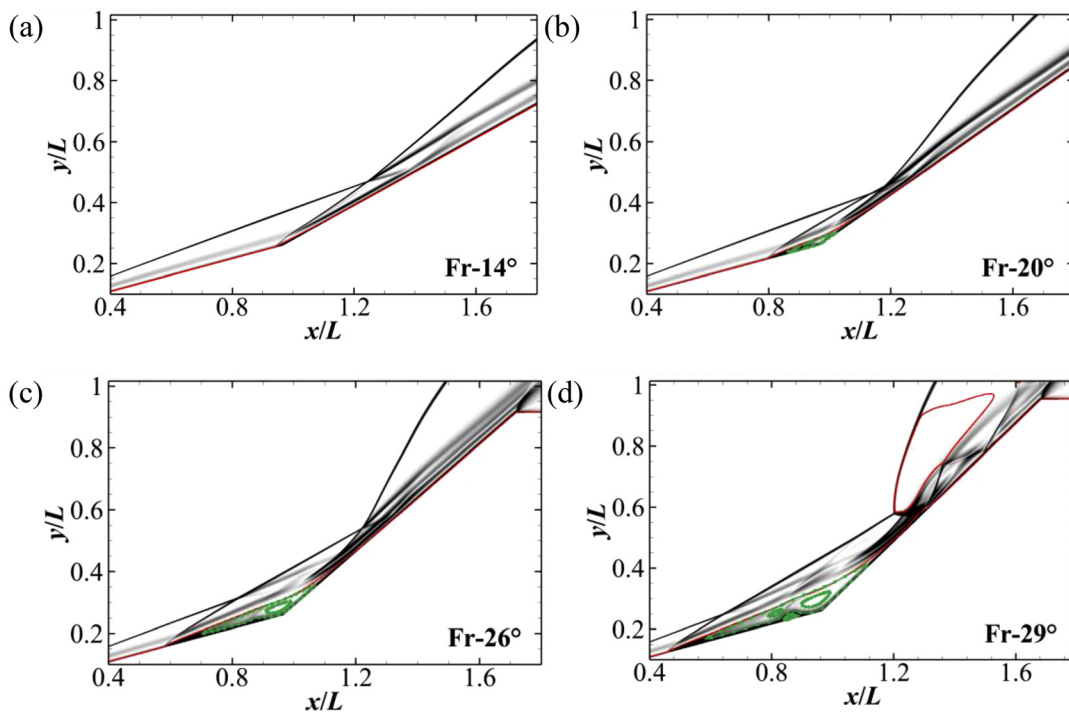


FIG. 4. Contours of the density gradient magnitude superimposed with streamlines (in green) and sonic lines (in red): (a) Fr-14°; (b) Fr-20°; (c) Fr-26°; and (d) Fr-29°.

and the enthalpy of formation. As a result, the translational temperature behind the curved shock decreases as vibrational excitation and dissociation are activated sequentially.

Figure 7 shows the contours of the mass fraction of species O, N, and NO for the TCN-26° case. A dissociation incubation region can be observed behind the curved shock, where vibrational excitation dominates with little dissociation. Further downstream, the mass fractions of atomic O and N reach their peak values between the curved shock and slip line. Atomic O can also be found in the separation region and the reattached boundary layer, whereas atomic N is absent from these regions due to the high dissociation energy threshold of N₂. As seen in Fig. 7(c), the distribution of NO formed due to the Zel'dovich mechanism resembles that of atomic O.

Figure 8 presents the distributions of the skin friction coefficient, surface Stanton number, and surface pressure coefficient at $\alpha = 14^\circ$ (incipient separation) and $\alpha = 26^\circ$ (secondary separation) for different thermochemistry models. The separation and reattachment points of the primary bubble are determined by the most upstream and downstream locations where C_f crosses zero. At $\alpha = 14^\circ$, the low post-shock translational temperature only induces weak thermochemical non-equilibrium. As a result, the distributions of surface quantities and the critical angles of incipient separation are almost identical for different models. At $\alpha = 26^\circ$, the inclusion of vibrational excitation and dissociation decreases the size of the separation region due to the same mechanism that decreases the shock standoff distance. The surface Stanton number behaves in a similar way to the skin friction. For both angles,

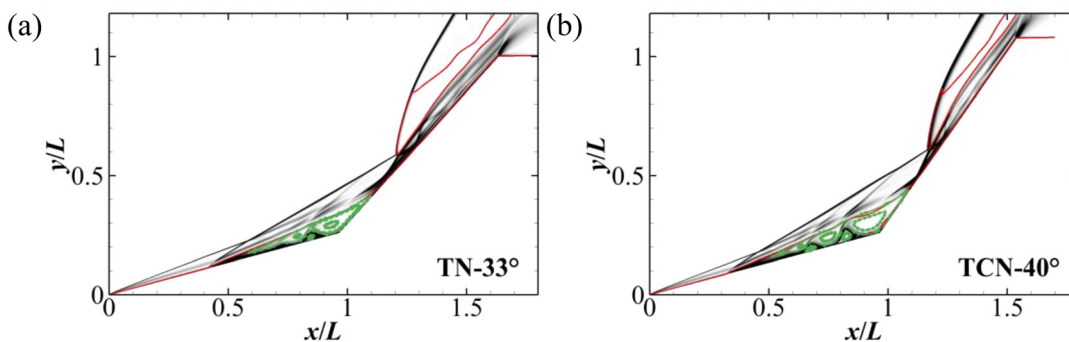


FIG. 5. Contours of the density gradient magnitude superimposed with streamlines (in green) and sonic lines (in red): (a) TN-33° and (b) TCN-40°.

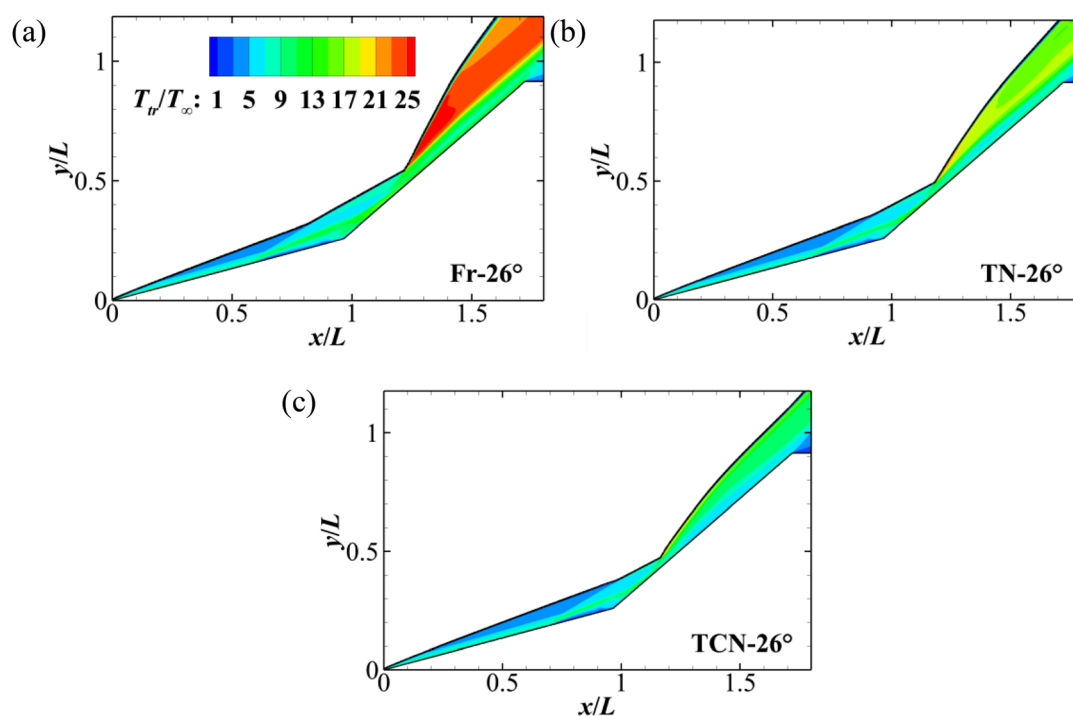


FIG. 6. Contours of the nondimensional translational temperature T_{tr}/T_{∞} : (a) Fr-26°; (b) TN-26°; and (c) TCN-26°. The black solid line represents the shock location.

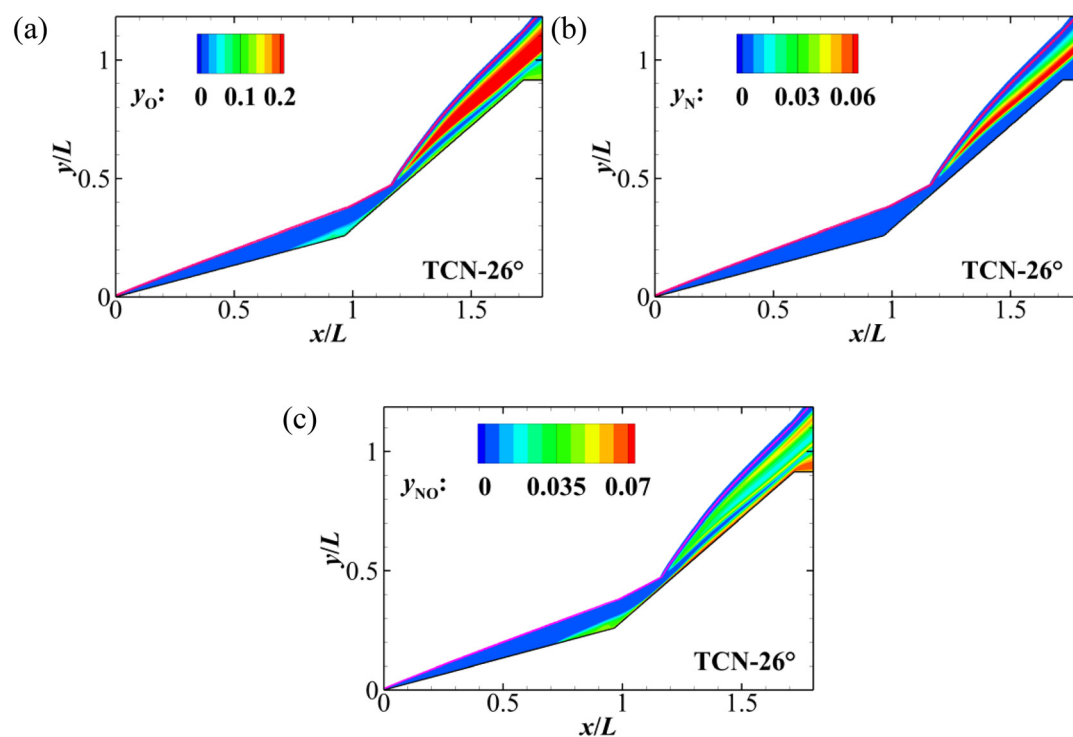


FIG. 7. Contours of the mass fraction of (a) O, (b) N, and (c) NO for TCN-26° superimposed with shock locations.

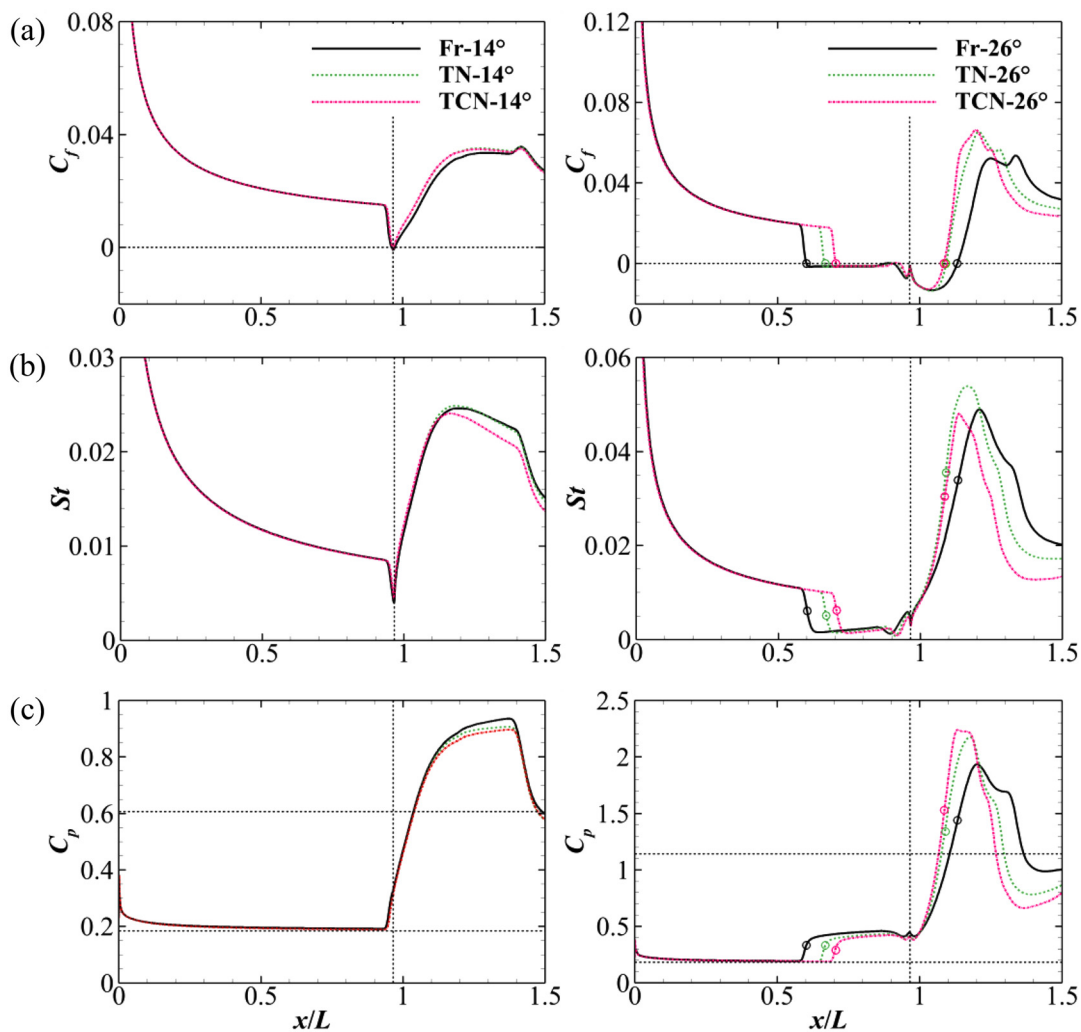


FIG. 8. Distributions of the (a) skin friction coefficient, (b) surface Stanton number, and (c) surface pressure coefficients at $\alpha = 14^\circ$ (left column) and $\alpha = 26^\circ$ (right column) for the Fr, TN, and TCN models. Open circles: separation and reattachment points of the primary bubble; vertical dashed line: corner; horizontal dashed line in (a): zero skin friction; horizontal dashed lines in (c): inviscid theory.

the pressure peak on the second wedge significantly exceeds the value predicted by inviscid theory, which is caused by hypersonic viscous interaction.¹ Far downstream of the corner, the pressure approaches the inviscid value. At $\alpha = 26^\circ$, the plateau pressure decreases as vibrational excitation and dissociation are accounted for, whereas the pressure peak shows the opposite trend.

As discussed by Gai and Khraibut⁴⁶ and Hao *et al.*,²² secondary separation is induced by an adverse pressure gradient, posed by the rotational motion of the primary bubble upon the reverse flow boundary layer, which manifests itself as the pressure “dip” near the corner. To further examine the thermochemical nonequilibrium effects on the adverse pressure gradient, Fig. 9 plots the contour of the nondimensional streamwise pressure gradient and its distribution along the surface at $\alpha = 26^\circ$ for different models. Here, s^* is the nondimensional distance along the model surface measured from the corner, with the negative sign representing the first wedge. The sudden increase in the

pressure gradient near the separation point of the primary bubble is caused by the separation shock. The pressure gradient remains nearly zero inside the pressure plateau and decreases to a negative value near the corner, which is caused by the footprint of the low pressure in the vortex core of the primary bubble. For different models, the negative peaks are of similar magnitude, which explains the similar critical angles for secondary separation.

B. Onset of global instability

To investigate the thermochemical nonequilibrium effects on the global instability of high-enthalpy double-wedge flows with respect to three-dimensional perturbations, GSA is performed on two-dimensional base flows over a wide range of spanwise wavelengths.

Figure 10 shows the growth rates of the least stable modes captured by the GSA for the Fr, TN, and TCN models. The peak growth

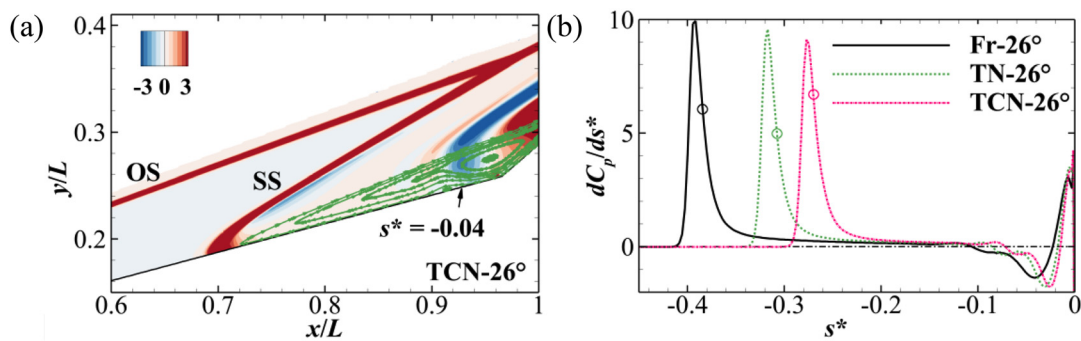


FIG. 9. (a) Contour of the nondimensional streamwise pressure gradient superimposed with streamlines for TCN-26°; (b) distributions of the streamwise gradient of the surface pressure coefficient along the model surface for Fr-26°, TN-26°, and TCN-26°. Open circles: separation points of the primary bubble; horizontal line: zero pressure gradient.

rates and the corresponding wavelengths are also plotted against α for different models. When α is small, the flow is globally stable with negative growth rates for all spanwise wavelengths. Global instability first appears at $\alpha = 19^\circ$ for the Fr and TN models, whereas its occurrence for the TCN model is slightly postponed to $\alpha = 20^\circ$. In these cases, the

least stable modes are stationary ($\omega_r = 0$), which belong to the same family labeled mode 1. As α is increased, the maximum growth rate increases, and the corresponding wavelength is shifted to a larger value. Similar behaviors of the onset of global instability were observed for supersonic compression corner flows in a calorically perfect gas.²² Near the critical α , the flow is slightly stabilized by thermal and chemical nonequilibrium; however, the difference between the peak growth rates predicted by different models diminishes as α is increased. The least unstable spanwise wavelength increases with α but decreases with the inclusion of thermal and chemical nonequilibrium, which indicates that the wavelength of the global instability scales with the length of the separation region.¹⁹

Figure 11 presents the contours of the real parts of spanwise velocity perturbation w' (left column) and translational temperature perturbation T'_{tr} (right column) of mode 1 superimposed with the shock locations and dividing streamlines at $\alpha = 20^\circ$ for the Fr, TN, and TCN models. The separation and reattachment points are marked by closed circles. It is confirmed that these modes are of the same nature for different thermochemical nonequilibrium models, although the length of the separation region varies greatly. Similar to previous GSA studies of supersonic flow over double wedges and compression corners,^{19,21,22} w' and T'_{tr} are present both inside the separation region and along the reattached boundary layer, which is responsible for the formation of counterrotating streamwise vortices and streamwise streaks in surface heating rates.²¹

Hereafter, we focus on the global instability of the TCN-26° case, where the GSA identifies several stationary and oscillatory unstable modes. Figure 12 shows the growth rates of the unstable modes as a function of spanwise wavelength. As λ_z/L approaches 0.2 from the right, mode 1 and another stationary mode (mode 5) move toward each other along the imaginary axis. Then, the two modes with pure real eigenvalues leave the imaginary axis to form oscillatory mode 2 and its conjugate mode. As λ_z/L is further decreased to 0.1, mode 2 and its conjugate mode move back to the imaginary axis to form stationary modes 3 and 6. Eventually, the flow becomes stable for small values of λ_z/L . Note that the most unstable mode is mode 2 for the TCN-26° case, with the growth rate peaking at $\lambda_z/L = 0.1337$. The corresponding frequency is approximately $f = 2.86$ kHz ($fL/u_\infty = 0.044$), which is much lower than the flow characteristic frequency. There is another oscillatory mode (mode 4) with a small growth rate.

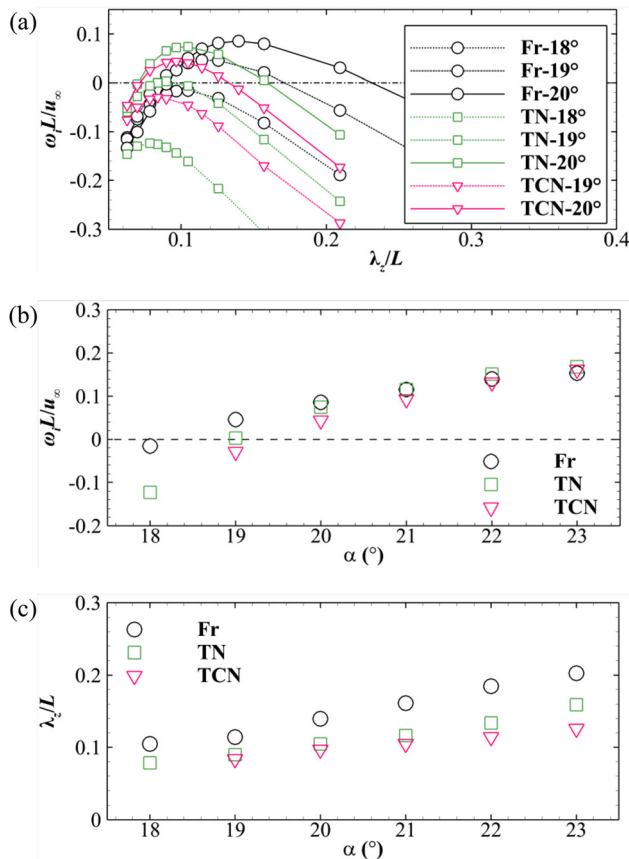


FIG. 10. Variations in (a) the growth rates of mode 1 as a function of spanwise wavenumber, (b) the peak growth rates of mode 1, and (c) the corresponding spanwise wavelengths as a function of α for the Fr, TN, and TCN models.

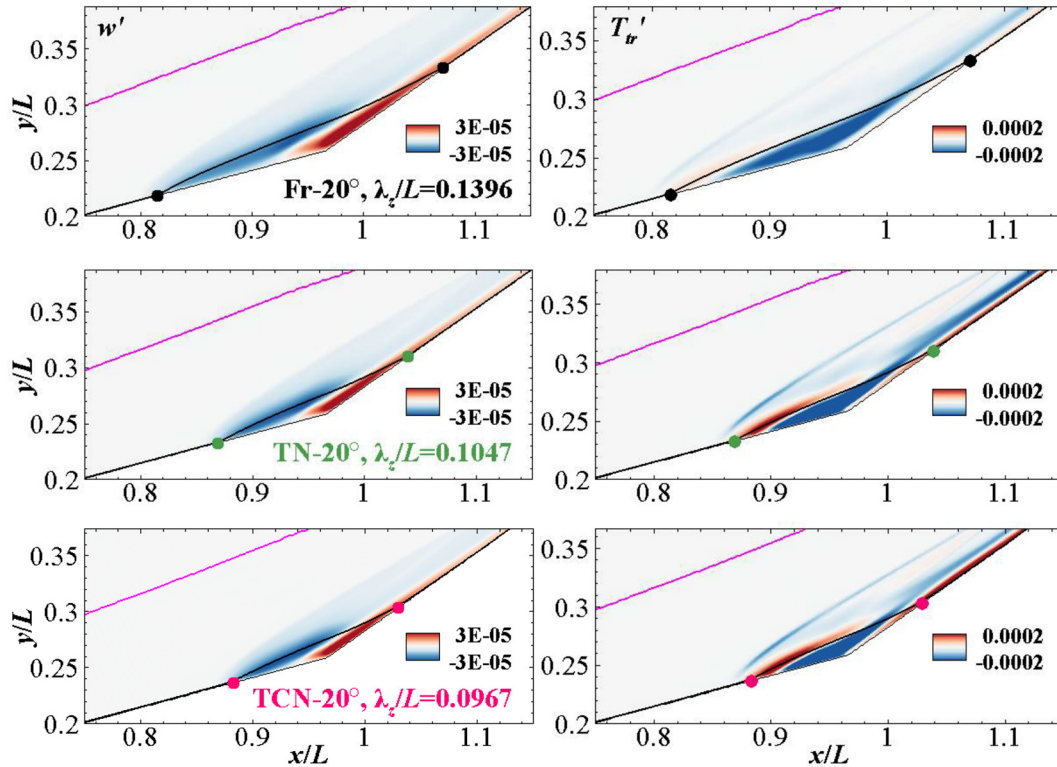


FIG. 11. Contours of the real parts of spanwise velocity perturbation w' (left column) and translational temperature perturbation T'_{tr} (right column) of mode 1 superimposed with shock locations (in magenta) and dividing streamlines (in black) corresponding to the most unstable modes at $\alpha = 20^\circ$ for the Fr, TN, and TCN models.

The contours of the real parts of spanwise velocity perturbation w' and translational temperature perturbation T'_{tr} are shown in Fig. 13 for modes 1–3 at their respective most unstable perturbation wavelengths for the TCN-26° case. Modes 1 and 3 structurally resemble the long-wavelength and short-wavelength unstable modes beyond a critical deflection angle found in supersonic compression corner flows.²² As expected, mode 2 shares some of the same features as modes 1 and 3. A similar oscillatory mode was also reported for supersonic compression corner flows, which, however, did not dominate over the short-wavelength mode.²²

The thermochemical nonequilibrium effects can act on global instability in two ways. First, the base flows are altered by the inclusion

of vibrational excitation and dissociation, as discussed in Sec. IV A. Second, the perturbations can also undergo thermochemical nonequilibrium processes, which is accounted for by the Jacobian of the source terms in the GSA. To examine which mechanism is more relevant, the eigenvalue spectra obtained with and without the source Jacobian at the most unstable wavelength of mode 2 are compared in Fig. 14 for the TCN-26° case. The two spectra almost overlap, which indicates that the perturbations are thermochemically frozen. It can be speculated that the bulk viscosity due to vibrational nonequilibrium plays a negligible role in global instability. The role of rotational nonequilibrium requires further examinations.

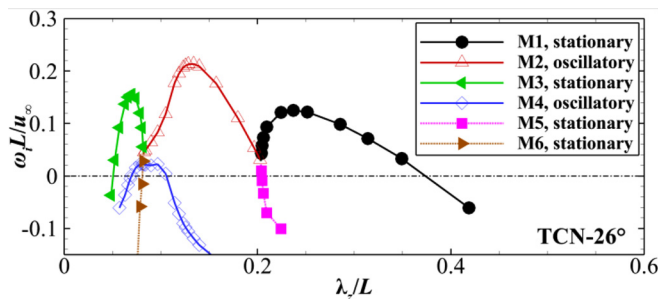


FIG. 12. Growth rates of the unstable modes as a function of spanwise wavelength for TCN-26°.

C. Comparison with triple-deck theory

The Navier–Stokes formulation of shock-induced separation can be reduced into a single-parameter boundary value problem governed by the incompressible boundary-layer equations according to the classical triple-deck theory.^{47,48} In the triple-deck formulation of the supersonic laminar flow over a compression corner, the only governing parameter is the scaled deflection angle,

$$\alpha^* = \frac{\alpha Re_L^{1/4}}{C^{1/4} \lambda^{1/2} (M_e^2 - 1)^{1/4}}, \quad Re_L = \frac{\rho_e u_e L}{\mu_e}, \quad C = \frac{\mu_w T_e}{\mu_e T_w}, \quad (12)$$

where α is the deflection angle in radians, Re_L is the Reynolds number based on the flow properties at the edge of the incoming boundary

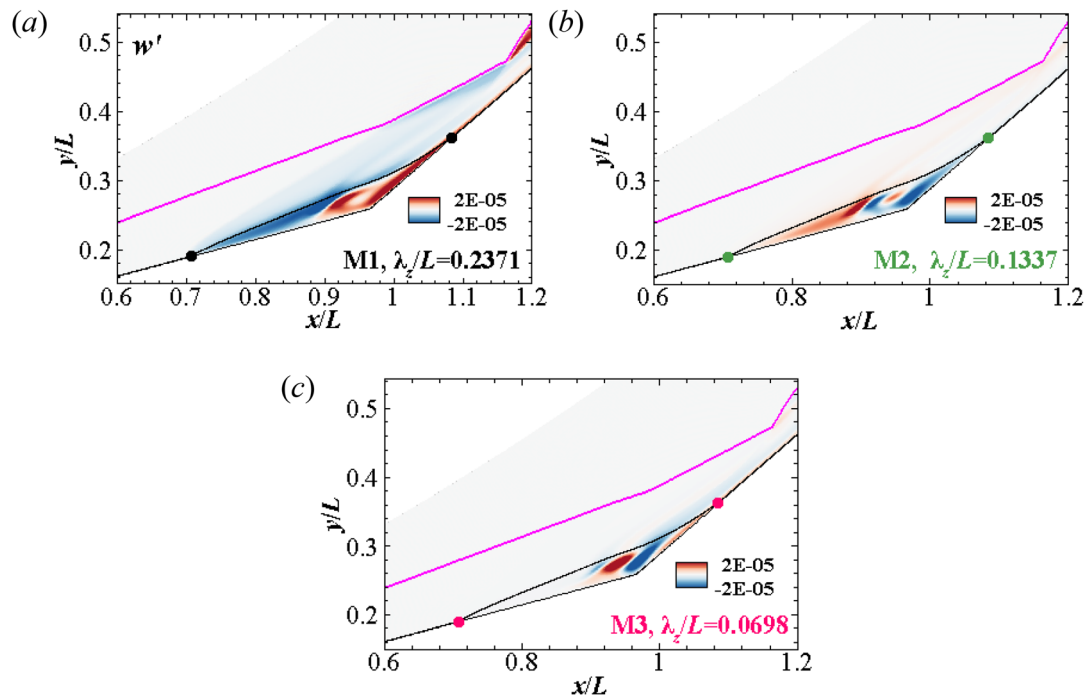


FIG. 13. Contours of the real parts of spanwise velocity perturbation w' superimposed with shock locations (in magenta) and dividing streamlines (in black) for (a) mode 1, (b) mode 2, and (c) mode 3 at the most unstable wavelengths for TCN-26°.

layer (denoted by the subscript e) and L , μ is the dynamic viscosity, C is the Chapman–Rubesin parameter, the subscript w denotes properties at the wall, and λ is a value determined by the slope of the velocity profile at the wall in the incoming boundary layer and equals 0.3322 for a Blasius boundary layer. In this study, the flow properties at the edge of the incoming boundary layer are determined using oblique shock relations in a calorically perfect gas for the Fr, TN, and TCN models, given that only weak vibrational excitation and nearly no chemical reactions occur behind the shock induced by the first wedge as seen in Fig. 7. This is also supported by Fig. 8, where the

distributions of the surface quantities predicted by different models are overlapped.

Figure 15 examines the variations in the nondimensional length of the separation region L_{sep}/L as a function of $\alpha^{*3/2}$ for the Fr, TN, and TCN models, where L_{sep} is the axial distance between the separation and reattachment points. The Fr, TN, and TCN results approximately lie on straight lines, albeit with different slopes, which is consistent with the analysis of Burggraf⁴⁹ and Korolev *et al.*⁵⁰ based on

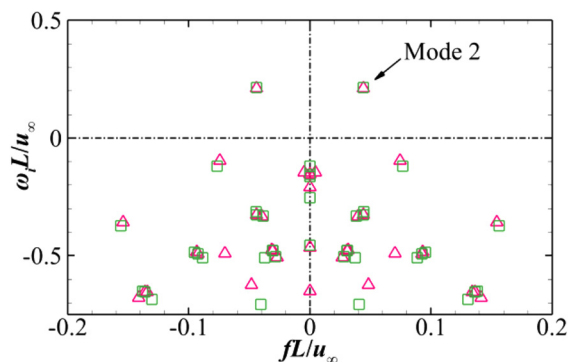


FIG. 14. Eigenvalue spectra at the most unstable spanwise wavelength $\lambda_z/L = 0.1337$ of mode 2 for TCN-26° with and without the source Jacobian represented by squares and triangles, respectively.

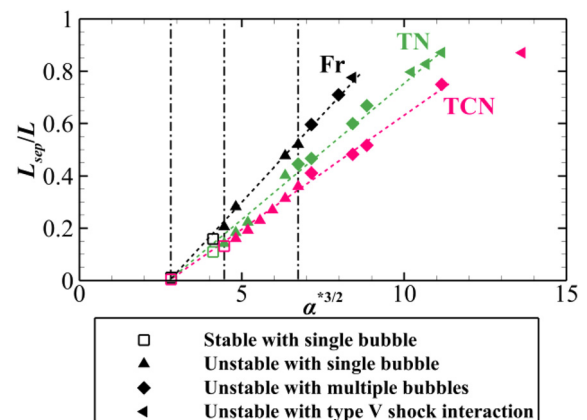


FIG. 15. Variation in the nondimensional length of separation L_{sep}/L as a function of $\alpha^{*3/2}$ for the Fr, TN, and TCN models. The three vertical lines indicate the onset of incipient separation, global instability, and secondary separation.

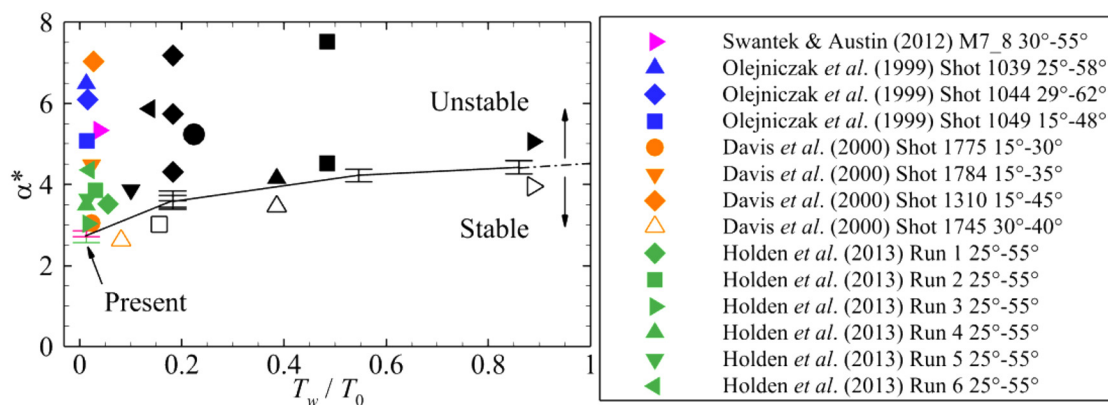


FIG. 16. Critical scaled deflection angle for global instability as a function of wall to total temperature ratio. The black symbols were taken from Hao *et al.*²² for supersonic compression corner and double-wedge flows in a calorically perfect gas.

Neiland's reattachment theory.⁴⁷ Interestingly, the linear relation still holds for thermochemical nonequilibrium flows. From left to right, the three vertical lines indicate the onset of incipient separation, global instability, and secondary separation at $\alpha^* \approx 2.00$, 2.71, and 3.57. The critical angle for incipient separation is greater than the triple-deck value of 1.57,^{51,52} whereas that for secondary separation is lower than the triple-deck value of 4.5.^{50,53} These behaviors are caused by cold-wall effects.^{22,54}

More importantly, the criterion for the global instability boundary proposed by Hao *et al.*²² can be extended to thermochemical nonequilibrium flows with a low wall-to-total temperature ratio, as shown in Fig. 16. The black symbols were taken from Hao *et al.*²² for supersonic compression corner and double-wedge flows in a calorically perfect gas. The present result follows the previous downward trend as T_w/T_0 is decreased, which indicates that high-enthalpy flow is more prone to global instability than its cold-flow counterpart. The values of α^* corresponding to the high-enthalpy double-wedge and double-cone experiments of Swantek and Austin,⁵⁵ Olejniczak *et al.*,⁴ Davis and Sturtevant,⁵⁶ and Holden *et al.*⁸ are calculated and added to this figure. Note that λ equals $0.332\sqrt{3}$ for double-cone flows according to the Mangler transformation. All double-cone runs conducted in the LENS XX expansion tunnel are globally unstable. In other words, these flows are expected to be intrinsically three-dimensional and even unsteady. Three-dimensional simulations should be performed to reproduce the experiments.

V. CONCLUSIONS

Hypersonic laminar flow over double wedges is investigated using CFD and GSA with different thermochemistry models, including the frozen, thermal nonequilibrium, and thermochemical nonequilibrium models. The base-flow CFD analysis solves the two-dimensional Navier–Stokes equations with a two-temperature model for thermal nonequilibrium and a five-species reacting air model for chemical nonequilibrium.

Vibrational excitation and dissociation absorb the translational energy into the internal and chemical energy modes, which affects the flow through changes in translational temperature and density. The thermochemical nonequilibrium effects tend to reduce the standoff distance of the curved shock induced by the second wedge and the size

of the separation bubble and, thus, delay the pulsation mode of the shock interaction system. However, the onset of incipient separation and secondary separation is unaffected.

The GSA reveals that the flow becomes unstable with respect to spanwise periodic perturbations beyond a similar critical value of deflection angle for different models. The thermochemical nonequilibrium effects slightly stabilize the flow mainly through altering the base flow, whereas the perturbations are almost thermochemically frozen. The numerical data are interpreted using classical triple-deck scaling. High-enthalpy shock-induced separated flows are more prone to global instability than their cold-flow counterparts. It is suggested that high-enthalpy SWBLI experiments should be conducted in the globally stable regime to exclude the influence of flow three-dimensionality.

ACKNOWLEDGMENTS

This work was supported by the Hong Kong Research Grants Council (Nos. 15206519 and 25203721), the National Natural Science Foundation of China (Nos. 12102377, 11372325, and 91116013), and the Strategic Priority Research Program of Chinese Academy of Sciences (No. XDA17030100). The authors would also like to thank Dr. Xiaoye Sherry Li for her valuable advice on setting tuning parameters for Super-LU.

AUTHOR DECLARATIONS

Conflict of Interest

The authors have no conflicts to disclose.

DATA AVAILABILITY

The data that support the findings of this study are available from the corresponding author upon reasonable request.

APPENDIX: VALIDATION OF THE THERMOCHEMICAL NONEQUILIBRIUM GSA SOLVER

Our in-house finite-volume GSA solver in a calorically perfect gas has been previously validated^{21–23} and is extended to thermochemical nonequilibrium effects in this study. To validate the new

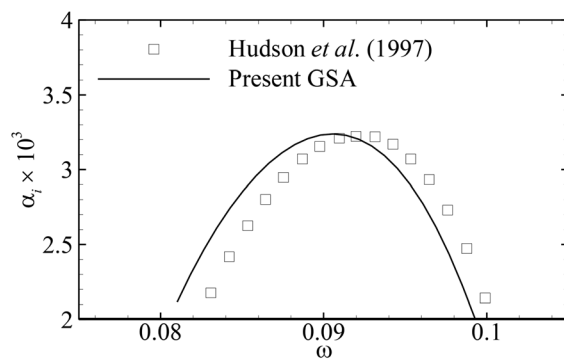


FIG. 17. Growth rates of the second mode in a Mach 10 flow over a cold-wall flat plate.

solver, the temporal instability of the second mode is analyzed in a Mach 10 flow of air in thermochemical nonequilibrium over a cold-wall flat plate. The boundary layer is assumed to be parallel, which enables a periodic boundary condition in the streamwise direction. The spanwise wavenumber is set to zero. The temporal results are then processed by the Gaster transformation,⁵⁷ which is an accurate approximation for weakly unstable modes.⁵⁸ The resulting spatial growth rates of the second mode are compared to the LST predictions of Hudson *et al.*¹⁵ at $x = 0.4$ m measured from the leading edge of the flat plate, as shown in Fig. 17. Here, α_i and ω represent the streamwise growth rate and the angular frequency nondimensionalized using the free-stream properties and a reference length $x/\sqrt{Re_x}$. Good agreement is obtained with almost the same peak growth rates except for a slight shift in frequency with the relative difference less than 5%. This is because different thermochemical nonequilibrium models were used to generate the base flows.

REFERENCES

- ¹H. Babinsky and J. K. Harvey, *Shock Wave-Boundary-Layer Interactions* (Cambridge University Press, 2011).
- ²G. H. Furumoto, X. Zhong, and J. C. Skiba, "Numerical studies of real-gas effects on two-dimensional hypersonic shock-wave/boundary-layer interaction," *Phys. Fluids* **9**(1), 191–210 (1997).
- ³S. G. Mallinson, S. L. Gai, and N. R. Mudford, "The interaction of a shock wave with a laminar boundary layer at a compression corner in high-enthalpy flows including real gas effects," *J. Fluid Mech.* **342**, 1–35 (1997).
- ⁴J. Olejniczak, G. V. Candler, M. J. Wright, I. Leyva, and H. G. Hornung, "Experimental and computational study of high enthalpy double-wedge flows," *J. Thermophys. Heat Transfer* **13**(4), 431–440 (1999).
- ⁵M. S. Holden and T. P. Wadhams, "A database of aerothermal measurements in hypersonic flow in 'building block' experiments for CFD validation," AIAA Paper No. 2003-1137, 2003.
- ⁶I. Nompelis and G. V. Candler, "Investigation of hypersonic double-cone flow experiments at high enthalpy in the LENS facility," AIAA Paper No. 2007-0203, 2007.
- ⁷M. Maclean and M. S. Holden, "Numerical assessment of data in catalytic and transitional flows for Martian entry," AIAA Paper No. 2006-2946, 2006.
- ⁸M. S. Holden, M. Maclean, T. P. Wadhams, and A. Dufrene, "Measurements of real gas effects on regions of laminar shock wave/boundary layer interaction in hypervelocity flows for 'blind' code validation studies," AIAA Paper No. 2013-2837, 2013.
- ⁹N. Kianvashrad and D. Knight, "Nonequilibrium effects on prediction of aerothermodynamic loading for a double cone," *AIAA J.* **57**(7), 2946–2963 (2019).
- ¹⁰M. E. Holloway, R. S. Chaudhry, and I. D. Boyd, "Assessment of hypersonic double-cone experiments for validation of thermochemistry models," *J. Spacecr. Rockets* **59**(2), 389–400 (2022).
- ¹¹C. Park, *Nonequilibrium Hypersonic Aerothermodynamics* (Wiley, New York, 1990).
- ¹²R. S. Chaudhry, I. D. Boyd, E. Torres, T. E. Schwartzentruber, and G. V. Candler, "Implementation of a chemical kinetics model for hypersonic flows in air for high-performance CFD," AIAA Paper No. 2020-2191, 2020.
- ¹³J. Gao, J. Hao, J. Wang, and C. Lee, "Effect of thermochemical nonequilibrium modeling on high-enthalpy double-cone flow," *J. Spacecr. Rockets* **58**(4), 1243–1247 (2021).
- ¹⁴M. R. Malik and E. C. Anderson, "Real gas effects on hypersonic boundary-layer stability," *Phys. Fluids A* **3**(5), 803–821 (1991).
- ¹⁵M. L. Hudson, N. Chokani, and G. V. Candler, "Linear stability of hypersonic flow in thermochemical nonequilibrium," *AIAA J.* **35**(6), 958–964 (1997).
- ¹⁶X. Chen, L. Wang, and S. Fu, "Parabolized stability analysis of hypersonic thermal-chemical nonequilibrium boundary-layer flows," *AIAA J.* **59**(7), 2382–2395 (2021).
- ¹⁷J. Robinet, "Bifurcations in shock-wave/laminar-boundary-layer interaction: Global instability approach," *J. Fluid Mech.* **579**, 85–112 (2007).
- ¹⁸V. Theofilis, "Global linear instability," *Annu. Rev. Fluid Mech.* **43**, 319–352 (2011).
- ¹⁹G. S. S. Sidharth, A. Dwivedi, G. V. Candler, and J. W. Nichols, "Onset of three-dimensionality in supersonic flow over a slender double wedge," *Phys. Rev. Fluids* **3**, 093901 (2018).
- ²⁰N. Hildebrand, A. Dwivedi, J. W. Nichols, M. R. Jovanović, and G. V. Candler, "Simulation and stability analysis of oblique shock-wave/boundary-layer interactions at Mach 5.92," *Phys. Rev. Fluids* **3**(1), 013906 (2018).
- ²¹S. Cao, J. Hao, I. Kliouchnikov, H. Olivier, and C. Y. Wen, "Unsteady effects in a hypersonic compression ramp flow with laminar separation," *J. Fluid Mech.* **912**, A3 (2021).
- ²²J. Hao, S. Cao, C.-Y. Wen, and H. Olivier, "Occurrence of global instability in hypersonic compression corner flow," *J. Fluid Mech.* **919**, A4 (2021).
- ²³J. Hao, J. Fan, S. Cao, and C.-Y. Wen, "Three-dimensionality of hypersonic laminar flow over a double cone," *J. Fluid Mech.* **935**, A8 (2022).
- ²⁴K. Sutton and P. A. Gnoffo, "Multi-component diffusion with application to computational aerothermodynamics," AIAA Paper No. 1998-2575, 1998.
- ²⁵F. G. Blottner, M. Johnson, and M. Ellis, "Chemically reacting viscous flow program for multi-component gas mixtures," Report No. SC-RR-70-754 (Sandia National Lab., Albuquerque, NM, 1971).
- ²⁶W. G. Vincenti and C. H. Kruger, *Introduction to Physical Gas Dynamics* (Krieger, 1965).
- ²⁷C. R. Wilke, "A viscosity equation for gas mixtures," *J. Chem. Phys.* **18**(4), 517–519 (1950).
- ²⁸R. C. Millikan and D. R. White, "Systematics of vibrational relaxation," *J. Chem. Phys.* **39**(12), 3209–3213 (1963).
- ²⁹P. A. Gnoffo, R. N. Gupta, and J. L. Shinn, "Conservation equations and physical models for hypersonic air flows in thermal and chemical nonequilibrium," Report No. 2867 (NASA, 1989).
- ³⁰T. K. Mankodi and R. S. Myong, "Quasi-classical trajectory-based non-equilibrium chemical reaction models for hypersonic air flows," *Phys. Fluids* **31**, 106102 (2019).
- ³¹N. Adhikari and A. A. Alexeenko, "A general form of Macheret–Fridman classical impulsive dissociation model for nonequilibrium flows," *Phys. Fluids* **33**, 056109 (2021).
- ³²Y. Gorbachev, O. Kunova, and G. Shoen, "A non-equilibrium dissociation and vibrational relaxation model for computational fluid dynamics simulations of flows with shock waves," *Phys. Fluids* **33**, 126105 (2021).
- ³³Q. Hong, X. Wang, Y. Hu, and Q. Sun, "Development of a stagnation streamline model for thermochemical nonequilibrium flow," *Phys. Fluids* **32**, 046102 (2020).
- ³⁴M. S. Grover and P. Valentini, "Ab initio simulation of hypersonic flows past a cylinder based on accurate potential energy surfaces," *Phys. Fluids* **33**, 051704 (2021).
- ³⁵B. E. Edney, "Effects of shock impingement on the heat transfer around blunt bodies," *AIAA J.* **6**(1), 15–21 (1968).

- ³⁶J. Olejniczak, M. J. Wright, and G. V. Candler, "Numerical study of inviscid shock interactions on double-wedge geometries," *J. Fluid Mech.* **352**, 1–25 (1997).
- ³⁷J. Hao, J. Wang, and C. Lee, "Numerical Study of hypersonic flows over reentry configurations with different chemical nonequilibrium models," *Acta Astronaut.* **126**, 1–10 (2016).
- ³⁸J. Hao and C.-Y. Wen, "Hypersonic flow over spherically blunted double cones," *J. Fluid Mech.* **896**, A26 (2020).
- ³⁹R. W. MacCormack, *Numerical Computation of Compressible and Viscous Flow* (AIAA, 2014).
- ⁴⁰B. Van Leer, "Towards the ultimate conservative difference scheme," *J. Comput. Phys.* **32**(1), 101–136 (1979).
- ⁴¹M. J. Wright, G. V. Candler, and D. Bose, "Data-parallel line relaxation method for the Navier–Stokes equations," *AIAA J.* **36**(9), 1603–1609 (1998).
- ⁴²D. Sorensen, R. Lehoucq, C. Yang, and K. Maschhoff, *ARPACK Software, Version 2.3* (SIAM, 1996).
- ⁴³X. S. Li, "An overview of SuperLU: Algorithms, implementation, and user interface," *ACM Trans. Math. Software* **31**(3), 302–325 (2005).
- ⁴⁴A. Mani, "Analysis and optimization of numerical sponge layers as a nonreflective boundary treatment," *J. Comput. Phys.* **231**, 704–716 (2012).
- ⁴⁵H. G. Hornung, R. J. Gollan, and P. A. Jacobs, "Unsteadiness boundaries in supersonic flow over double cones," *J. Fluid Mech.* **916**, A5 (2021).
- ⁴⁶S. L. Gai and A. Khraibut, "Hypersonic compression corner flow with large separated regions," *J. Fluid Mech.* **877**, 471–494 (2019).
- ⁴⁷V. Y. Neiland, "Theory of laminar boundary layer separation in supersonic flow," *Fluid Dyn.* **4**(4), 33–35 (1969).
- ⁴⁸K. Stewartson and P. G. Williams, "Self-induced separation," *Proc. R. Soc. A* **312**, 181–206 (1969).
- ⁴⁹O. R. Burggraf, "Asymptotic theory of separation and reattachment of a laminar boundary layer on a compression ramp," Report No. AGARD-CP-168 (AGARD, 1975).
- ⁵⁰G. L. Korolev, J. B. Gajjar, and A. I. Ruban, "Once again on the supersonic flow separation near a corner," *J. Fluid Mech.* **463**, 173–199 (2002).
- ⁵¹A. I. Ruban, "Numerical solution of the local asymptotic problem of the unsteady separation of a laminar boundary layer in a supersonic flow," *USSR Comput. Math. Math. Phys.* **18**(5), 175–187 (1978).
- ⁵²D. P. Rizzetta, O. R. Burggraf, and R. Jenson, "Triple-deck solutions for viscous supersonic and hypersonic flow past corners," *J. Fluid Mech.* **89**, 535–552 (1978).
- ⁵³F. T. Smith and A. F. Khorrami, "The interactive breakdown in supersonic ramp flow," *J. Fluid Mech.* **224**, 197–215 (1991).
- ⁵⁴I. V. Egorov, V. Y. Neiland, and V. V. Shvedchenko, "Three-dimensional flow structures at supersonic flow over the compression ramp," AIAA Paper No. 2011-0730, 2011.
- ⁵⁵A. B. Swantek and J. M. Austin, "Heat transfer on a double wedge geometry in hypervelocity air and nitrogen flows," AIAA Paper No. 2012-0284, 2012.
- ⁵⁶J. P. Davis and B. Sturtevant, "Separation length in high-enthalpy shock/boundary-layer interaction," *Phys. Fluids* **12**(10), 2661–2687 (2000).
- ⁵⁷M. Gaster, "A note on the relation between temporally-increasing and spatially-increasing disturbances in hydrodynamic stability," *J. Fluid Mech.* **14**, 222–224 (1962).
- ⁵⁸G. A. Brès, M. Inkman, T. Colonius, and A. V. Fedorov, "Second-mode attenuation and cancellation by porous coatings in a high-speed boundary layer," *J. Fluid Mech.* **726**, 312–337 (2013).